RSC Advances

PAPER

View Article Online
View Journal | View Issue

Check for updates

Cite this: *RSC Adv.*, 2025, **15**, 16635

Comparative study of ultraviolet absorption properties between iron selenide nanoparticles and zinc oxide nanoparticles based on first-principles calculations

Yuqi Gao,[ab] Dong Zhang, *[ab] Dingming Cao,[ab] Jing Bai,[ab] Kun Guo,[ab] Xiangyu Li,[ab] Haodong Yan,[ab] Yalong Chen[ab] and He Zhang[ab]

The intensification of global warming has exacerbated health risks associated with prolonged exposure to high-intensity ultraviolet (UV) radiation. Zinc oxide (ZnO), widely utilized as an inorganic physical sunscreen in commercial products, faces challenges such as significant photodegradation under prolonged UV exposure and limited absorption capacity primarily in the ultraviolet radiation A (UVA) range. These limitations necessitate the development of novel materials with enhanced UV absorption efficiency. In this context, iron selenide (FeSe), known for its metallic nature and broad UV absorption spectrum, emerges as a promising candidate. This study systematically investigates the UV absorption properties of FeSe nanoparticles (NPs) for the first time, comparing them with ZnO NPs through integrated experimental and first-principles theoretical approaches. Results demonstrate that FeSe exhibits superior UV absorption properties compared to ZnO, with a maximum absorption coefficient of 2.5×10^5 cm^{-1} at 220 nm. This work not only systematically investigates the UV absorption properties of FeSe for the first time but also establishes a theoretical and experimental foundation for designing stable, high-efficiency UV-absorbing materials.

Received 10th March 2025
Accepted 11th May 2025

DOI: 10.1039/d5ra01705j

rsc.li/rsc-advances

Open Access Article. Published on 19 May 2025. Downloaded on 6/7/2026 11:34:35 AM.
This article is licensed under a Creative Commons Attribution-NonCommercial 3.0 Unported Licence.

1 Introduction

High-intensity ultraviolet (UV) radiation poses severe health risks by penetrating the dermis, damaging elastic fibers, accelerating skin aging and increasing the likelihood of skin cancer.[1] Consequently, the development of advanced UV-absorbing materials is critical for safeguarding public health. Ideal UV-absorbing materials should exhibit low reflectivity, strong absorption capacity across a broad spectral range, and high environmental stability.

Zinc oxide nanoparticles (ZnO NPs) have emerged as functional nanomaterials due to their quantum size effects, high chemical reactivity, and effective UV absorption and scattering capabilities.[2,3] With a wide bandgap (E_g = 3.37 eV), ZnO efficiently absorbs UV radiation by converting it into scattered light,[4,5] making it a common ingredient in inorganic sunscreens.[6] However, the absorption of ZnO is predominantly limited to the ultraviolet radiation A (UVA) range (320–400 nm),[7] and its performance degrades significantly under prolonged UV exposure due to photodegradation.[8,9]

Iron selenide (FeSe), a transition metal chalcogenide, has recently attracted attention for its metallic properties, broad UV absorption spectrum, and resistance to photodegradation.[10,11] While FeSe is extensively studied for its superconducting properties,[12,13] its optical characteristics, particularly UV absorption, remain underexplored. Previous studies report that FeSe exhibits no optical bandgap from far-infrared to ultraviolet wavelengths, with a high absorption coefficient confirming its metallic behavior.[14] In addition, the study by Deng *et al.* demonstrated the conjugation of FeSe quantum dots with polyethylene glycol (PEG) and HER2 antibodies, enabling their specific targeting of HER2-overexpressing tumor cells. This functionalized nanostructure exhibits promising potential for application in multiphoton-based cancer imaging modalities due to its enhanced tumor-specific binding capability and optical properties suitable for advanced bioimaging techniques.[15,16] Notably, Lin *et al.* observed minimal impact of UV-induced photodegradation on FeSe's light absorption properties, despite effects on electrical properties.[17] As summarized in Table 1, prior studies have successfully synthesized FeSe nanomaterials with diverse morphologies through various methods. However, their UV absorption properties remain suboptimal.

First-principles calculations based on density functional theory (DFT) were employed to analyze the band structure,

[a]*College of Electrical and Electronic Engineering, Harbin University of Science and Technology, Harbin, Heilongjiang 150080, China. E-mail: zhangdong@hrbust.edu.cn*
[b]*Key Laboratory of Engineering Dielectric and Its Application, Ministry of Education, Harbin University of Science and Technology, Harbin, Heilongjiang 150080, China*

© 2025 The Author(s). Published by the Royal Society of Chemistry

Open Access Article. Published on 19 May 2025. Downloaded on 6/7/2026 11:34:35 AM. This article is licensed under a Creative Commons Attribution-NonCommercial 3.0 Unported Licence.

Table 1 Summary of synthesis methods and UV absorption properties of FeSe nanomaterials

Author	Synthesis method	Morphology	UV absorption range (nm)	Maximum absorbance (a.u.)
Deng *et al.*	Wet chemistry method[18]	FeSe hollow nanospheres	200–400	1.0
Ubale *et al.*	Chemical bath deposition[19]	FeSe thin films	340–400	1.83

electronic density of states (DOS) and optical properties of materials. The electronic structures and optical properties of FeSe and ZnO play a critical role in their potential applications in UV absorption. For instance, Xu *et al.* synthesized six ZnO nanocrystals with the shapes of granule, flake, rod, porous flake, nanosheet-assembled flower, and nanorod-assembled flower and investigated the correlation between their photocatalytic activities and morphological features. Their DFT calculations indicated that polar crystal planes could enhance charge carrier separation.[20] Similarly, Abdelghani *et al.* investigated the electronic band structure and DOS of wurtzite ZnO. By combining DFT with the generalized gradient approximation (GGA), they concluded that the valence band of ZnO arises from the hybridization of O-2p and Zn-3d orbitals.[21] In contrast, FeSe's electronic properties have been extensively investigated. Ghosh *et al.* performed DFT-based calculations on FeSe with a *P*4/*nmm* space group, revealing its low magnetization.[22] Additionally, Long *et al.* utilized first-principles calculations to study the electronic nematicity of FeSe.[23] Collectively, these studies demonstrate that theoretical analyses provide critical insights into the material properties of FeSe and ZnO. However, research on their electronic structures and optical properties, particularly their UV absorption mechanisms, remains limited, despite their potential for practical applications.

This study systematically investigated the UV absorption properties of FeSe for the first time. FeSe and ZnO nanoparticles (NPs) with average diameters of approximately 50 nm were synthesized *via* a solvothermal method. The structural, compositional, morphological, and optical properties were systematically investigated through a combination of X-ray diffraction (XRD), scanning electron microscopy (SEM), Fourier transform infrared spectroscopy (FTIR), and ultraviolet-visible spectroscopy (UV-Vis). Experimental results revealed distinct differences in electronic configurations and optical behaviors between the two nanomaterials. Furthermore, DFT-based first-principles calculations were conducted to examine their electronic structures and optical parameters. The integration of computational modeling with experimental measurements enabled a comprehensive understanding of the materials' properties. Detailed analysis of band structures and density of states (DOS) elucidated the dielectric functions and absorption coefficients, facilitating systematic comparison of their optical properties. Results demonstrated that FeSe NPs exhibit significantly enhanced UV absorption capabilities compared to ZnO NPs, achieving a maximum absorption coefficient of 2.5×10^5 cm^{-1} at 220 nm wavelength. This investigation not only addresses the existing research gap in the UV absorption of FeSe but also establishes a robust theoretical–experimental framework for developing advanced UV-absorbing materials.

2 Experimental and computational details

2.1 Experimental methods

The synthetic procedure is schematically illustrated in Fig. 1. Iron selenide (FeSe) and zinc oxide (ZnO) nanoparticles were synthesized *via* a solvothermal process. Two distinct 40 mL aqueous solutions were prepared: Solution A containing 0.06 mol sodium hydroxide (NaOH), 0.002 mol zinc chloride ($ZnCl_2$), and 0.006 mol sodium citrate dihydrate ($Na_3C_6H_5O_7 \cdot 2H_2O$); Solution B comprising 0.06 mol potassium hydroxide (KOH), 0.002 mol selenium powder (Se), and 0.002 mol ferric chloride hexahydrate ($FeCl_3 \cdot 6H_2O$). Each solution was magnetically stirred until complete dissolution of precursors. Subsequently, 10 mL hydrazine hydrate ($N_2H_4 \cdot H_2O$) was introduced into Solution B. Both solutions were then subjected to hydrothermal treatment at 180 °C for duration-specific periods (12 h for Solution A, 24 h for Solution B). The resultant suspensions, exhibiting a milky white appearance for ZnO (Solution A) and a black colloidal dispersion for FeSe (Solution B), were centrifuged at 8000 rpm, triple-washed with absolute ethanol, and finally dried at 60 °C for 8 h in a vacuum oven. The obtained products were mechanically ground using an agate mortar, yielding white ZnO and black FeSe powders respectively.

2.2 Characterization

Crystallographic analysis was performed by XRD with Cu Kα radiation (2θ = 10–90°, scan rate 10° min^{-1}). The microstructure of FeSe and ZnO NPs was characterized with a scanning electron microscope (SEM, Zeiss Gemini Sigma 300, Germany).

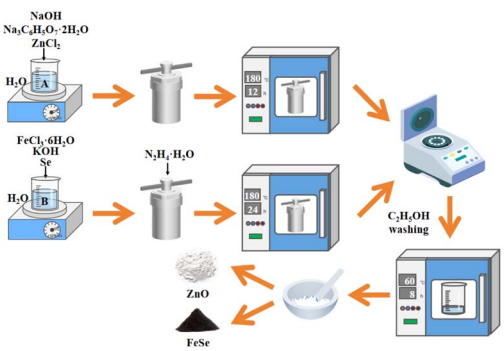

Fig. 1 Preparation process diagram.

© 2025 The Author(s). Published by the Royal Society of Chemistry

Open Access Article. Published on 19 May 2025. Downloaded on 6/7/2026 11:34:35 AM. This article is licensed under a Creative Commons Attribution-NonCommercial 3.0 Unported Licence.

FTIR spectroscopic measurements were conducted across the mid-infrared region (4000–400 cm^{-1}) to analyze the sample composition. The optical properties of the samples were investigated by using a UV-Vis spectrophotometer over the wavelength range of 200–400 nm.

2.3 Computational methods

First-principles calculations were conducted within the density functional theory (DFT) framework employing a plane-wave pseudopotential (PWP) approach, implemented in the CASTEP module (v2023) of Materials Studio software.[24] The Perdew–Burke–Ernzerhof (PBE) functional under the generalized gradient approximation (GGA) was selected to describe exchange–correlation interactions.[25] Norm-conserving pseudopotentials were adopted to model core electrons,[26] with valence configurations defined as Fe: $3d^64s^2$, Se: $4s^24p^4$, Zn: $3d^{10}4s^2$, and O: $2s^22p^4$. These valence electron configurations correspond to the neutral atomic states but are optimized to represent the ionic states in the compounds (Fe^{2+}, Se^{2-}, Zn^{2+}, O^{2-}) through pseudopotential design. This approach ensures accurate modeling of the electronic interactions in FeSe and ZnO.

The computational framework enabled systematic investigation of both bulk crystalline phases and surface configurations. Structural optimization was conducted by relaxing atomic positions and lattice parameters until energy and force criteria were met. The Broyden–Fletcher–Goldfarb–Shanno (BFGS) algorithm was employed for geometry optimization, with a *k*-point grid density of 6 × 6 × 6 to ensure convergence. The energy convergence threshold was set to 1×10^{-5} eV per atom, and the maximum force tolerance was 0.03 eV $Å^{-1}$. The kinetic energy cutoff was optimized to 600 eV through convergence testing to minimize Pulay stress artifacts.[27] This methodological approach facilitated comprehensive analysis of key optoelectronic parameters including band structure profiles, density of states (DOS) distributions, frequency-dependent dielectric functions, and wavelength-resolved absorption coefficients.

Band structure analysis serves as a fundamental theoretical construct for elucidating electronic state distributions and charge transport mechanisms in crystalline solids. This framework enables quantitative description of electron dynamics through Bloch wavefunction solutions to the Schrödinger equation in periodic potentials. Crucially, the enhancement of lattice periodicity induces progressive band splitting, leading to systematic bandgap expansion. The electron energy E and wave function $\Psi(x)$ in a one-dimensional periodic potential satisfy the Schrödinger eqn (1), where $\hbar$ is the reduced Planck constant, m is the electron mass, and $V(x)$ is the one-dimensional periodic potential:

$$-\frac{\hbar^2}{2m}\frac{d^2\Psi(x)}{dx^2} + V(x)\Psi(x) = E\Psi(x) \quad (1)$$

The optical properties of materials can be evaluated by calculating the variation of the dielectric function with photon frequency. Other properties can also be derived from the dielectric function using corresponding relationships. The functional expression for the complex dielectric function $\varepsilon(\omega)$ is as follows:[28]

$$\varepsilon(\omega) = \varepsilon_1(\omega) + i\varepsilon_2(\omega) \quad (2)$$

Here, ω represents the photon frequency, $\varepsilon_1(\omega)$ is the real part of the dielectric function, $\varepsilon_2(\omega)$ is the imaginary part, and P denotes the principal value. The real part can be derived from the analysis of the Kramers–Kronig dispersion relation, while the imaginary part can be obtained by deriving the matrix elements between the occupied and unoccupied states of the electron wave functions. The absorption coefficient $\alpha(\omega)$ can be derived from the real part $\varepsilon_1(\omega)$ and the imaginary part $\varepsilon_2(\omega)$, with the functional expression given below:[29,30]

$$\varepsilon_1(\omega) = \frac{2}{\pi}P\int_0^\infty \frac{\omega'\varepsilon_2(\omega')d\omega'}{\left(\omega'^2 - \omega^2\right)'} + 1 \quad (3)$$

$$\varepsilon_2(\omega) = -\frac{2\omega}{\pi}P\int_0^\infty \frac{\varepsilon_1(\omega')}{\omega'^2 - \omega^2}d\omega' \quad (4)$$

$$\alpha(\omega) = \sqrt{2}\omega\left[\sqrt{\varepsilon_1^2(\omega) + \varepsilon_2^2(\omega)} - \varepsilon_1(\omega)\right]^{\frac{1}{2}} \quad (5)$$

3 Results and discussion

3.1 Structural and compositional analysis

3.1.1 Atomic structure models. The crystallographic configurations of FeSe and ZnO are comparatively presented in Fig. 2. FeSe crystallizes in the tetragonal system with the space group *P*4/*mmm*, while ZnO crystallizes in the hexagonal system with the space group $P6_3mc$. As shown in Fig. 2(a), the Se^{2-} in FeSe occupy the body center, face center, and edge center positions, with each Fe^{2+} surrounded by four Se^{2-}. The structural visualization in Fig. 2(b) reveals the Zn and O atoms in ZnO alternate in a planar arrangement within the hexagonal lattice, with the larger atoms being Zn. The original cell parameters of FeSe and ZnO were obtained from their respective standard crystallographic databases (FeSe: PDF #97-063-347; ZnO: PDF #36-1451). To refine the atomic configurations, structural optimization was performed *via* DFT calculations using the CASTEP module with the GGA-PBE functional. The detailed unit cell parameters and those after structural optimization are listed in Table 2.

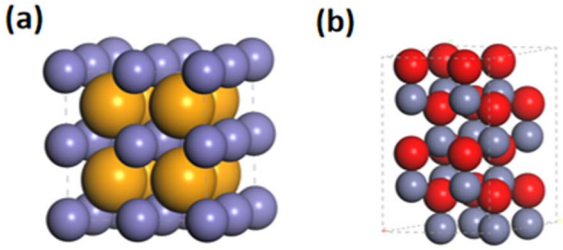

Fig. 2 Crystal structure diagram for (a) FeSe and (b) ZnO.

Open Access Article. Published on 19 May 2025. Downloaded on 6/7/2026 11:34:35 AM. This article is licensed under a Creative Commons Attribution-NonCommercial 3.0 Unported Licence.

Table 2 Cell parameters and structure optimized cell parameters

		Original parameters				Structure optimization parameters			
Material name	Space group	a/Å	b/Å	c/Å	V/Å^3	a/Å	b/Å	c/Å	V/Å^3
FeSe	$P4/mmm$	2.956	2.956	4.730	41.330	2.967	2.967	2.934	25.828
ZnO	$P6_3mc$	3.249	3.249	5.206	54.955	3.256	3.256	5.285	56.029

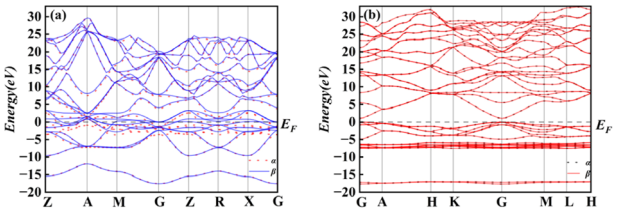

Fig. 3 Band structure of (a) FeSe and (b) ZnO.

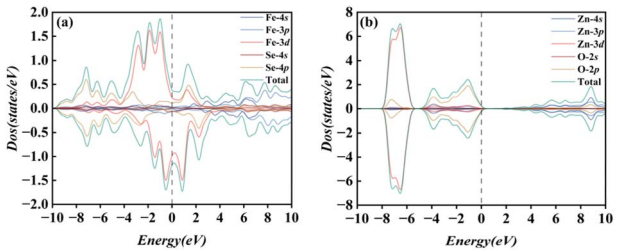

Fig. 4 Density of states and partial density of states for (a) FeSe and (b) ZnO.

3.1.2 Density of states distribution of electrons. Fig. 3 presents the comparative band structures of FeSe and ZnO within the energy window spanning −20 eV to 33 eV relative to the Fermi level (E_F = 0 eV). For FeSe (Fig. 3(a)), the degenerate conduction band minimum (CBM) and valence band maximum (VBM) exhibit complete overlap at the G point, characteristic of metallic behavior with zero bandgap. Spin-resolved analysis reveals non-degenerate α (spin-up) and β (spin-down) states across the Brillouin zone, confirming the material's intrinsic magnetism through spin polarization energies exceeding 0.5 eV. In contrast, ZnO (Fig. 3(b)) demonstrates a direct bandgap of 1.026 eV at the G point between CBM and VBM, with computational results exhibiting the well-documented density functional theory (DFT) bandgap underestimation effect (experimental value: 3.37 eV) inherent to the generalized Gradient Approximation plus U method (GGA+U). This systematic error originates from incomplete cancellation of electron self-interaction energies in the exchange–correlation functional, though the relative energy level alignment remains physically consistent for optical analysis. However, this does not affect the analysis of the material's optical properties. Furthermore, the spin-degenerate electronic states (α−β overlap < 0.01 eV) in ZnO confirm its non-magnetic nature. In contrast, FeSe exhibits a VBM closer to the E_F, enabling more efficient electron transitions within the UV energy range and a higher transition probability. Due to the lack of a band gap, electrons in FeSe require very little energy to transition from the valence band to the conduction band, resulting in stronger UV absorption properties.

To elucidate the electronic structure characteristics, Fig. 4 presents comparative analyses of total and partial density of states (DOS) for FeSe and ZnO, with all energy values referenced to their intrinsic Fermi levels. FeSe exhibits continuous distributions of occupied and unoccupied states, with the Fermi level positioned within this continuous energy spectrum, confirming its metallic characteristics. In contrast, ZnO demonstrates distinct separation between occupied and unoccupied states, accompanied by a symmetrical DOS distribution that verifies its direct band gap semiconductor nature. This fundamental difference originates from their distinct electronic configurations: Zn^{2+} in ZnO possesses a fully filled d^{10} configuration, leading to semiconducting behavior, whereas Fe^{2+} in FeSe (d^6 configuration) exhibits metallic properties due to partially filled d orbitals. Such electronic configuration disparity directly governs their photoexcitation mechanisms: ZnO relies on interband transitions, while FeSe's continuous density of states enables low-energy electron transitions, thereby enhancing UV absorption. This observation aligns with the well-established correlation between d-electron orbital filling and optical properties in transition metal compounds.[31] Pronounced orbital hybridization occurs between Fe-3d and Se-4p orbitals within the energy range of −8.0 to 2.0 eV, while Zn-3*d* and O-2p orbitals show analogous hybridization from −4.0 to 0.0 eV, facilitating covalent bond formation. Notably, FeSe possesses significantly higher electronic state density at both VBM and CBM compared to ZnO. This configuration promotes enhanced electron excitation under UV irradiation. The broad energy level distribution enables electron population across multiple states, generating an extended absorption band that substantiates the superior UV absorption properties of FeSe.

3.1.3 Morphological study. The crystal structures of the samples were analyzed by XRD. Fig. 5 shows the XRD patterns of FeSe and ZnO nanoparticles (NPs). The diffraction main peaks of FeSe NPs at 2θ = 18.732°, 30.191°, 35.808°, 38.108°, 43.261°, 58.914°, 62.717°, and 67.228° can be well indexed to the (001), (100), (101), (002), (110), (112), (200), and (103) planes of FeSe (PDF #97-063-347). The strong diffraction peaks of the ZnO NPs at 2θ = 31.786°, 34.476°, 36.269°, 47.552°, 56.594°, 62.871°, 67.952°, and 69.110° were attributed to the (100), (002), (101), (102), (110), (103), (112), and (201) planes of ZnO (PDF #36-1451).

© 2025 The Author(s). Published by the Royal Society of Chemistry

Open Access Article. Published on 19 May 2025. Downloaded on 6/7/2026 11:34:35 AM.
This article is licensed under a Creative Commons Attribution-NonCommercial 3.0 Unported Licence.

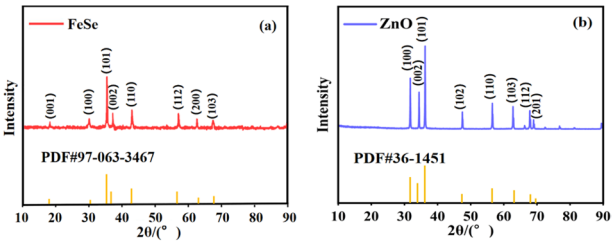

Fig. 5 XRD pattern of (a) FeSe and (b) ZnO.

Fig. 6 presents SEM micrographs elucidating the morphological characteristics of FeSe and ZnO NPs. FeSe NPs demonstrate well-defined tetragonal prism morphology with cross-sectional dimensions of 35 ± 2 nm and vertical growth extending to 50 ± 3 nm, consistent with *P*4/*mmm* space group symmetry. Conversely, ZnO NPs adopt hexagonal prism configurations exhibiting 20 ± 1.5 nm basal plane dimensions and 60 ± 2 nm axial lengths, in agreement with $P6_3mc$ space group classification. Quantitative analysis through volume-equivalent diameter calculations yields average particle sizes of 49.0 nm (FeSe) and 49.2 nm (ZnO), demonstrating comparable dimensional scaling between the two systems.

These morphological observations establish direct correlation with XRD phase identification results. The congruent structural parameters validate the efficacy of the solvothermal synthesis method in producing phase-pure FeSe and ZnO NPs with targeted crystallographic symmetries under specified reaction conditions.

3.1.4 Compositional analysis. The Fourier transform infrared (FTIR) spectra of the samples, measured in the range of 4000–400 cm^{-1}, are shown in Fig. 7. The as-prepared FeSe and ZnO exhibit strong infrared absorption peaks at 495 cm^{-1}, 582 cm^{-1}, 1627 cm^{-1}, and 3439 cm^{-1}. The sharp peaks at 495 cm^{-1} and 582 cm^{-1} are attributed to the stretching vibrations of Zn–O and Fe–Se bonds, respectively.[32,33] The intense absorption band at 1627 cm^{-1} arises from the C=O stretching vibration induced by carbon dioxide (CO_2) adsorption.[34] Hydroxyl groups (–OH) are evidenced by the broad band at 3439 cm^{-1}, indicating surface-adsorbed water (H_2O) on the nanoparticles.[35] These results suggest that the detected H_2O and CO_2 in both FeSe and ZnO samples likely originated from environmental exposure during synthesis and measurement.

3.2 Optical absorption properties analysis

UV-Vis absorption spectroscopy probes electronic transitions between valence and conduction bands. Fig. 8 comparatively illustrates the UV spectral responses (200–400 nm) of FeSe and ZnO, the *x*-axis represents wavelength, and the *y*-axis represents absorbance. FeSe displays featureless broadband absorption throughout the UV regime, consistent with the free-electron excitation mechanism inherent to metallic materials. Although hybridization occurs between the Fe-3d orbitals (with an empty E_g state) and Se-4p orbitals, the metallic nature of FeSe governs its absorption behavior, which is dominated by collective oscillations of multi-body electrons rather than the local charge transfer (CT) process from Fe to Se. Consequently, no distinct CT absorption peak is observed near 400 nm. This observation aligns with the electronic structure analysis (Section 3.1.2), where the overlapping conduction and valence bands enable continuous electronic transitions, distinct from the discrete interband transitions or CT mechanisms typical of semiconductors. In marked contrast, the absorbance curve of ZnO exhibits a bell shape with a distinct CT absorption peak at a wavelength of 372 nm. These results strongly indicate that FeSe demonstrates higher absorbance and a broader absorption range compared to ZnO, confirming FeSe's superior UV absorption properties. Furthermore, the FeSe NPs synthesized *via* the solvothermal method in this work demonstrate enhanced absorbance when compared with previously reported UV absorption properties of FeSe nanomaterials.

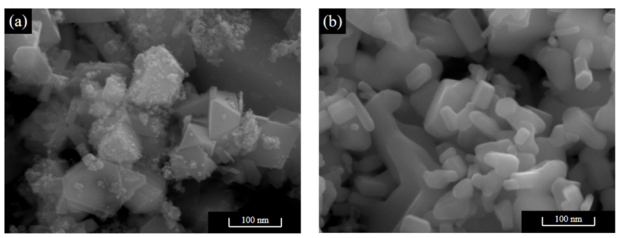

Fig. 6 SEM pattern of (a) FeSe and (b) ZnO.

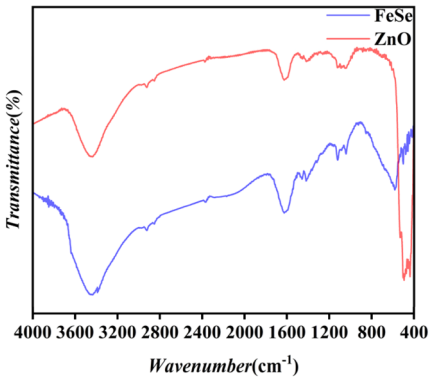

Fig. 7 FTIR spectra of FeSe and ZnO.

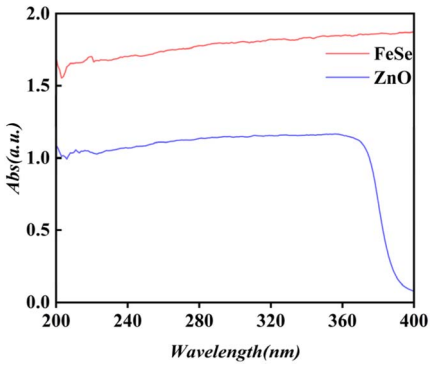

Fig. 8 Absorption spectra of FeSe and ZnO.

3.3. Calculation results of optical properties

3.3.1 Dielectric function. The dielectric function is one of the key properties of UV-absorbing materials, reflecting their

Open Access Article. Published on 19 May 2025. Downloaded on 6/7/2026 11:34:35 AM.
This article is licensed under a Creative Commons Attribution-NonCommercial 3.0 Unported Licence.

response to external electric fields. The real part of the dielectric function indicates the polarization degree of the material under UV, and its magnitude is related to the material's ability to store electrical energy. The imaginary part of the dielectric function represents the energy loss of the material under UV, which is related to its UV absorption capacity. A larger imaginary part indicates a stronger UV absorption capacity of the material. The dielectric function not only reflects the relationship between the solid's band structure and optical spectra,[36] but also serves as a bridge connecting interband transitions and the solid's electronic structure.

This investigation systematically evaluates the anisotropic dielectric response of FeSe and ZnO across principal crystallographic orientations (001), (010), and (100) in the UV spectrum. Fig. 9 compares the complex dielectric functions ($\varepsilon(\omega) = \varepsilon_1(\omega) + i\varepsilon_2(\omega)$) for both materials. Notably, equivalent dielectric behavior emerges between (010) and (100) planes (Fig. 9(b)), arising from cubic symmetry equivalence in these crystallographic directions. FeSe exhibits characteristic metallic dielectric signatures with $\varepsilon_1(\omega) < 0$ throughout the UV range, indicative of dominant free-electron screening effects. Conversely, ZnO demonstrates positive $\varepsilon_1(\omega)$ values, revealing enhanced dipole polarization capabilities with electric energy storage density. Both materials exhibit positive $\varepsilon_2(\omega)$ values, yet FeSe demonstrates a significantly higher magnitude in the dielectric imaginary part compared to ZnO within the UV range. This disparity in magnitude suggests that FeSe possesses a more pronounced energy dissipation mechanism and superior UV photoexcitation capabilities. Notably, the imaginary dielectric component of FeSe consistently lies above its real dielectric curve, forming a characteristic strong dispersion response profile, whereas ZnO's imaginary dielectric component remains entirely below its real part, reflecting conventional weak dispersion behavior. This intrinsic contrast directly reveals FeSe's markedly enhanced dielectric loss properties relative to ZnO. The underlying mechanism stems from FeSe's ability to achieve more efficient photothermal energy conversion through multiple relaxation processes under UV irradiation. This unique characteristic endows FeSe with dual advantages in UV shielding applications: it not only amplifies light absorption cross-sections by enhancing local field effects but also effectively suppresses UV transmittance through intensified non-radiative transitions, thereby realizing synergistic light-energy regulation capabilities.

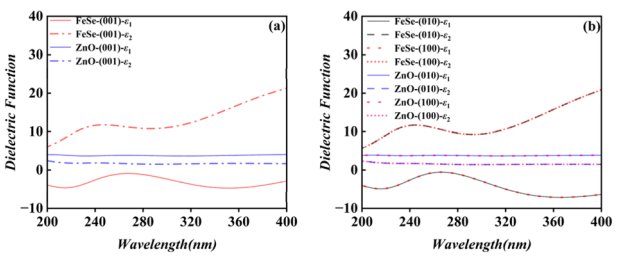

Fig. 9 Dielectric functions of FeSe and ZnO, (a) the (001) plane, (b) the (010) and (100) planes.

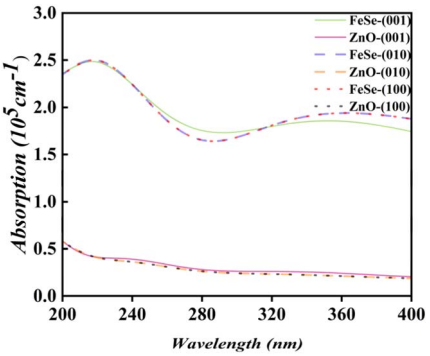

Fig. 10 Absorption coefficients of FeSe and ZnO.

3.4 Absorption coefficient

Fig. 10 shows the absorption coefficients of FeSe and ZnO within the UV range (200–400 nm) in the (001), (010), and (100) planes. Both materials exhibit equivalent absorption values along (010) and (100) planes, a direct consequence of their cubic lattice symmetry. Based on the trend of the absorption coefficient curve, the peak positions of the absorption coefficient roughly coincide with the peaks of the imaginary part of the dielectric function. The maximum absorption coefficient of FeSe reaches 2.5×10^5 cm^{-1} at a wavelength of 220 nm, while the absorption coefficient of ZnO decreases gradually as the wavelength increases, with a maximum value of 0.55×10^5 cm^{-1} at 200 nm. Comparing the absorption coefficients of FeSe and ZnO reveals that FeSe has a larger absorption coefficient and a broader absorption range than ZnO, demonstrating that FeSe exhibits stronger UV absorption properties and has the potential to be an efficient UV-absorbing material.

4 Conclusions

In this paper, we systematically investigate the UV absorption properties of FeSe for the first time, comparing them with those of ZnO, a commonly used UV-absorbing material. FeSe and ZnO nanoparticles were synthesized by controlling the reaction conditions of the solvothermal method. And it can be drawn from XRD and SEM that FeSe and ZnO are nanoparticles with tetragonal prism and hexagonal prism shapes, with average sizes of 49.0 nm and 49.2 nm, respectively. The UV-Vis measurement shows that, in the UV range (200–400 nm), FeSe has a greater absorbance and a wider absorption range than ZnO. In addition, the first-principles calculations based on DFT have been performed to systematically analyze the electronic structures and optical properties of FeSe and ZnO, with a comparative analysis of their optical properties through calculations of band structures, density of states, dielectric functions, and absorption coefficients. The results indicated that FeSe exhibits superior ultraviolet absorption properties compared to ZnO, with its maximum absorption coefficient reaching 2.5×10^5 cm^{-1} at a wavelength of 220 nm, demonstrating its potential as an efficient UV-absorbing material. These findings provide a theoretical foundation for designing

© 2025 The Author(s). Published by the Royal Society of Chemistry

Open Access Article. Published on 19 May 2025. Downloaded on 6/7/2026 11:34:35 AM. This article is licensed under a Creative Commons Attribution-NonCommercial 3.0 Unported Licence.

novel UV-absorbing materials and advance interdisciplinary research in optoelectronic materials.

Data availability

The authors confirm that all data supporting the findings of this study are fully presented within the main text of the manuscript.

Author contributions

Yuqi Gao: writing – review & editing, writing – original draft, investigation, formal analysis, data curation. Dong Zhang: supervision, funding acquisition, conceptualization, formal analysis, Data curation. Dingming Cao: writing – original draft, formal analysis, data curation. Jing Bai: formal analysis, data curation. Kun Guo: visualization, data curation. Xiangyu Li: visualization, investigation. Haodong Yan: visualization, investigation. Yalong Chen: visualization. He Zhang: visualization.

Conflicts of interest

There are no conflicts to declare.

Acknowledgements

This work was supported by the collaborative innovation achievements project of the "Double First-Class" disciplines in Heilongjiang Province (LJGXCG2023-092).

References

1 X. Cui, L. Yang, X. Gao, L. Jiang, Y. Guan and L. Ma, Synthesis and Performance Study of Triazine-based UV Absorbers Containing Thiophene Structures, *Fine Petrochem.*, 2022, **04**, 22–26.
2 N. Mohammed, S. H. Nawar, M. S. Etawy, G. E. Nassar and A. G. Hassabo, Nanotechnology and its applications in industry and product design, *J. Text. Color. Polym. Sci.*, 2024, **21**, 273–284.
3 S. Singh, J. V. Gade, D. K. Verma, B. Elyor and B. Jain, Exploring ZnO nanoparticles: UV-visible analysis and different size estimation methods, *Opt. Mater.*, 2024, **152**, 115422.
4 B. Flores, M. Guzman, O. Chumpitaz, S. Flores, A. Rodriguez and J. E. Herrera, Crystallographic and optical properties of ZnO nanoparticles prepared by two different methods, *Appl. Phys. A*, 2025, **131**, 1–13.
5 K. Singha, S. Maity and P. Pandit, UV Protection *via* Nanomaterials, *Front. Text. Mater.*, 2020, 153–166.
6 S. Sahu and M. Bhattacharjee, Nanostructured ZnO thin film-based flexible printed sensor for high-performance UV detection, *Sens. Actuators, A*, 2025, **383**, 116196.
7 J. C. Hubaud, D. Guerin, M. Di Salvo, J. E. Branka, K. Mekideche and P. P. Pr, Real facts about safety and efficacy of zinc oxide and titanium dioxide in solar products, *J. Cosmet., Dermatol. Sci. Appl.*, 2021, **11**, 253–262.
8 S. Sheikhi, M. Aliannezhadi and F. S. Tehrani, Effect of precursor material, pH, and aging on ZnO nanoparticles synthesized by one-step sol-gel method for photodynamic and photocatalytic applications, *Eur. Phys. J. Plus*, 2022, **137**, 60.
9 M. Senthil Kumar and C. Arunagiri, Efficient photocatalytic degradation of organic dyes using Fe-doped ZnO nanoparticles, *J. Mater. Sci.: Mater. Electron.*, 2021, **32**, 17925–17935.
10 X. W. Wang, X. Y. Jiang, R. Z. Zhang, Z. Y. Zhao, X. J. Wei and Q. H. Chen, Electronic doping enhanced two-dimensionality of FeSe, *Sci. China:Phys., Mech. Astron.*, 2023, **53**, 214–221.
11 D. Scarpa, C. Cirillo, E. Ponticorvo, C. Cirillo, C. Attanasio, M. Iuliano and M. Sarno, Iron selenide particles for high-performance supercapacitors, *Materials*, 2023, **16**, 5309.
12 H. S. Xu and W. Xie, Synthesis methods, basic physical properties, and potential applications of the FeSe superconductor, *Coord. Chem. Rev.*, 2024, **501**, 215591.
13 Y. Wang, J. Lian, M. Wei, Y. Shi, K. Jin, C. Wang, Y. Zhang, Z. Xu, X. Zhou and Y. Li, Optical property and pseudogap study of FeSe thin films on different substrates, *Opt. Mater.*, 2022, **131**, 112727.
14 X. J. Wu, D. Z. Shen, Z. Z. Zhang, J. Y. Zhang, K. W. Liu, B. H. Li, Y. M. Lu, B. Yao, D. X. Zhao, B. S. Li, C. X. Shan, X. W. Fan, H. J. Liu and C. L. Yang, On the nature of the carriers in ferromagnetic FeSe, *Appl. Phys. Lett.*, 2007, **90**, 112105.
15 H. Kang, Y. Choi, M. Wei, J. Kwon, H.-Q. Nguyen, S. Lee, K. Kim, M. Lee and J. Lee, Optimizing scalable synthesis of high-quality FeSe quantum dot in organic and aqueous states, *Chem. Eng. J.*, 2023, **473**, 145034.
16 J. Kwon, S. W. Jun, S. I. Choi, X. Mao, J. Kim, E. K. Koh, Y.-H. Kim, S.-K. Kim, D. Y. Hwang, C.-S. Kim and J. Lee, FeSe quantum dots for *in vivo* multiphoton biomedical imaging, *Sci. Adv.*, 2019, **5**, eaay0044.
17 J. Lin, Q. Zhang, P. Tong, X. Zhang, X. Zhu, T. Shi, W. Lu, J. Chen, Y. Wu, H. Lu, L. He, B. Bai, Y. Jiang, W. Song and Y. Sun, Strain regulated giant negative thermal expansion in hexagonal sulfides $(Ni_{1-x}Fe_x)_{1-\delta}S$, *Appl. Phys. Lett.*, 2024, **124**, 221902.
18 Y. Deng, D. Li, X. Ning, D. Zhang, S. Zhang, Z. Zhang, D. Shan, Z. Wang, D. Liu, X. Mao and X. Lu, Self-Assembly of Biocompatible FeSe Hollow Nanostructures and 2D CuFeSe Nanosheets with One-and Two-Photon Luminescence Properties, *Small*, 2019, **15**, 1900627.
19 A. U. Ubale, Y. S. Sakhare, M. V. Bhute, M. R. Belkhedkar and A. Singh, Size-dependent structural, electrical and optical properties of nanostructured iron selenide thin films deposited by Chemical Bath Deposition Method, *Solid State Sci.*, 2013, **16**, 134–142.
20 H. Y. Xu, S. Q. Zhang, Y. F. Wang, Y. Xu, L. M. Dong and S. Komarneni, New insights into the photocatalytic mechanism of pristine ZnO nanocrystals: From experiments to DFT calculations, *Appl. Surf. Sci.*, 2024, **614**, 156225.
21 G. M. Abdelghani, A. Ben Ahmed and A. B. Al-Zubaidi, Prediction of electronic structure and nonlinear optical

Open Access Article. Published on 19 May 2025. Downloaded on 6/7/2026 11:34:35 AM.
This article is licensed under a Creative Commons Attribution-NonCommercial 3.0 Unported Licence.

properties of zinc oxide nanostructures by experimental characterization and theoretical investigation, *J. Electroceram.*, 2023, **51**, 179–191.

22 A. Ghosh, P. Chudzinski and M. Grüning, First-principles study and mesoscopic modeling of two-dimensional spin and orbital fluctuations in FeSe, *Phys. Rev. Res.*, 2024, **6**, 043154.

23 X. Long, S. Zhang, F. Wang and Z. Liu, A first-principle perspective on electronic nematicity in FeSe, *npj Quantum Mater.*, 2020, **5**, 50.

24 G. M. Quindoza, Y. Nakagawa, H. L. Mizuno, Y. Anraku, R. Espiritu and T. Ikoma, Site preference and local structural stability of Bi^{3+} substitution in hydroxyapatite using first-principles simulations, *Phys. Chem. Chem. Phys.*, 2024, **26**, 14277–14287.

25 B. Thakur, X. Gong and A. Dal Corso, Thermodynamic properties of fcc lead: A scalar and fully relativistic first principle study, *Comput. Mater. Sci.*, 2025, **249**, 113677.

26 S. M. Butorin, S. Bauters, L. Amidani, A. Beck, A. Rossberg, S. Weiss, T. Vitova, K. O. Kvashnina and O. Tougait, Effect of carbon content on electronic structure of uranium carbides, *Sci. Rep.*, 2023, **13**, 20434.

27 H. J. Monkhorst and J. D. Pack, Special points for Brillouin-zone integrations, *Phys. Rev. B*, 1976, **13**, 5188.

28 M. Y. An, Q. Xie, H. S. Zhang and Q. Liang, First-principles study of Mg doping at different concentrations in monolayer Janus WSS-e, *J. At. Mol. Phys.*, 2024, **41**, 130–136.

29 E. Ozugurlu, Cd-doped ZnO nanoparticles: An experimental and first-principles DFT studies, *J. Alloys Compd.*, 2021, **861**, 158620.

30 M. K. Gora, A. Kumar, S. Kumar, P. K. Maheshwari, D. Patidar, S. N. Dolia and R. K. Singhal, Electronic, optical and magnetic properties of Cu-doped ZnO, a possible system for eco-friendly and energy-efficient spintronic applications, *Environ. Sci. Pollut. Res.*, 2023, **30**, 98632–98646.

31 Z. N. Jaf, H. A. Miran, I. H. Khaleel and K. A. Jasim, Assessing the optoelectronic performance of d-orbital doped cubic HfO_2: The case of W, Nb, and Mo, *Optik*, 2022, **264**, 169341.

32 F. Qiao, Z. Wang, K. Xu and S. Ai, Double enzymatic cascade reactions within FeSe–Pt@SiO_2 nanospheres: synthesis and application toward colorimetric biosensing of H_2O_2 and glucose, *Analyst*, 2015, **140**, 6684–6691.

33 K. Sowri Babu, A. Ramachandra Reddy, C. Sujatha, K. Venugopal Reddy and A. N. Mallika, Synthesis and optical characterization of porous ZnO, *J. Adv. Ceram.*, 2013, **2**, 260–265.

34 W. Ma, Y. Feng, L. Wang, Y. Li, M. Shi and H. Cui, $Co_2(OH)_3Cl$ nanoparticles as new-type electrode material with high electrochemical performance for application in supercapacitor, *Adv. Powder Technol.*, 2017, **28**, 2642–2647.

35 S. Palanisamy and S. Srinivasan, Electrochemical reduction of CO_2 on $Ni(OH)_2$ doped water dispersible graphene under different electrolyte conditions, *SN Appl. Sci.*, 2019, **1**, 837.

36 X. C. Shen, *Spectral and Optical Properties of Semiconductors*, Science Press, Beijing, 2002.

© 2025 The Author(s). Published by the Royal Society of Chemistry